Liu *et al. Int J Concr Struct Mater* (2021) 15:2
https://doi.org/10.1186/s40069-020-00441-w

International Journal of Concrete Structures and Materials

RESEARCH Open Access

Experimental Investigation of the Mechanical Behaviour of Wall–Beam–Strut Joints for Prefabricated Underground Construction

Tingjin Liu[1,2,3,4*], Jiandong Lu[3], Di Wang[3] and Hongyuan Liu[4]

Abstract

Prefabricated construction is becoming increasingly prevalent, however, it is rarely applied in underground constructions, except for tunnel linings, due to the difficulties that arise in jointing various prefabricated components in underground conditions. To solve the vertical location problem of embedded mechanical couplers during the construction of wall–beam–strut joints for a prefabricated metro station, a new connection using welded steel plates is proposed. In this paper, four full-scale specimens of wall–beam–strut joints connected using welded steel plates and mechanical couplers were experimentally tested under monotonic and low-reversed cyclic loading conditions. The testing results were analysed in terms of the ultimate bearing capacity, failure mode, hysteresis, skeleton curve, stiffness degradation, energy dissipation and strain of the reinforcement bars. Notably, the two kinds of joints had similar ultimate bearing capacities and failure modes, but the crack distributions on the tops of the waler beams were different. For the specimens with the welded steel plate connection, tensile horizontal cracks first appeared on the top surface of the beam, where the welded steel plate was located, and then coalesced gradually; however, this cracking pattern was not observed during the experimental test of the specimens connected with the mechanical couplers. Furthermore, it was determined that the energy dissipation and ductility of the welded steel plate connection were better than those of the mechanical coupler connected joint, because the steel plate could redistribute the internal force in the joint and increase the stiffness. It was concluded that the proposed welded steel plate connection could be more favourable than the mechanical coupler connection in the construction of a prefabricated metro station in Guangzhou. Moreover, the results obtained from these experiments could provide guidelines for the corresponding connections employed in underground-prefabricated structures.

Keywords: prefabricated metro station, welded steel plate connection, low-reversed cyclic loading, full-scale test

1 Introduction

Prefabricated construction, also called modular construction, is a new construction technique in which building components are prefabricated in manufacturing factories and then assembled at construction sites (Gibb 1999; Jaillon and Poon 2009; Taylor 2010). Prefabricated construction originated from the late European colonial period and the post First World War period when numerous temporary and emergent prefabricated structures, such as houses and schools, were built (Pons 2014); however, prefabricated construction has received extensive attention in recent decades with the development of large construction machines. With the advantages of low energy consumption, high construction quality and reduced labour forces required at construction sites,

*Correspondence: Liu_tingjin@163.com
[1] State Key Laboratory of Subtropical Building Science, South China University of Technology, Guangzhou 510640, China
Full list of author information is available at the end of the article
Journal information: ISSN 1976-0485 / eISSN2234-1315

prefabricated construction has developed rapidly around the world in recent decades. Prefabricated housing was expected to reach 140,000 units in 2017 (Gibb 2007). Moreover, the State Council of the People's Republic of China advocated that, in the next decade, the proportion of buildings built with prefabricated construction should reach 30% (SCC (The State Council of the People's Republic of China) 2016). Therefore, with the rapid economic development and enhanced public awareness of environmental protection, prefabricated construction will be important in future building construction trends. In addition, the proportion of prefabricated construction has gradually become an important index for evaluating the level of a country's building construction industrialization.

Limited by construction machines, complex underground construction conditions and higher demands for seismic resistance and water resistance, prefabricated construction has rarely been applied in constructing underground structures other than tunnel linings. However, advances in science and technology, especially high-precision construction machines, create the possibility for prefabricated underground construction. As the most important part of an underground metro tunnel system, metro station prefabrication has attracted the attention of domestic construction enterprises, and some research institutions have carried out creative and exploratory studies. For example, a single-ring prefabricated metro station was proposed by Yang et al. (2017), Yang and Huang (2018). Five proposed metro stations have been successfully constructed and put into operation along Changchun Subway Line No. 2 in 2018. This proposed underground metro station design consists of seven prefabricated blocks, which have with tongue-and-groove joints solidified by slurry. Yang et al. (2019a, b) also investigated the influence of geometrical parameters on the mechanical performance of grouted mortise-tenon joints (MT·G-joints) used for the prefabricated underground stations and developed a shear capacity calculation method for the MT·G-joints based on the experimental results. To optimize the design of a prefabricated metro station, Ding et al. (2018, 2019a) studied the force transfer and deformation mechanism of the station using ABAQUS and proposed some effective optimum suggestions. Tao et al. (2019) conducted large-scale shaking table tests of the single-ring prefabricated subway station mentioned above. Their results showed that the single-ring prefabricated subway station had an excellent seismic performance. Furthermore, Ding et al. (2019b) analysed the seismic responses of the prefabricated metro station through ABAQUS and concluded that the prefabricated station showed better resistance to deformations compared with the traditional cast-in-place station. Their numerical results further revealed that the tiny deformations between the different structural components of the prefabricated metro station could effectively absorb the seismic effects caused by earthquakes. Jinanqiao Station of Beijing Subway Line No. 6 is a cut-and-cover subway station with the application of assembled monotonic technology (Du et al. 2017). The bottom slab of the station is cast-in-place, but the columns and sidewalls are precast, which are connected to the cast-in-place part by grout sleeves. Yanmazhuang West Station of Jinan Subway Line No. 1 is also a cut-and-cover subway station with an internally braced support system (Wang et al. 2018), which was designed with a combination of permanent structures and temporary supports. During the construction of this station, the prefabricated slabs were combined with the cast-in-place slab, and the permanent columns were combined with post-pouring temporary pillars. Moreover, the prefabricated underground construction process can avoid waste and demolition and save resources, which makes it a sustainable development strategy, and it is foreseeable that prefabricated buildings will be used for constructing future underground structures.

To improve construction speeds and convenience, welded steel plate connections are usually used in precast RC structure joints, and the mechanical behaviour of this kind of joint has been studied by many researchers. Kallolil et al. (1998) investigated the mechanical behaviour of three typical cast-in-site embedded steel plate joints. The connections were subjected to vertical and horizontal loads. Their results indicated that the failure of the joint was mainly caused by the yielding of the anchors and plates. Choi et al. (2013) experimentally studied four half-scale precast beam-column joints using a novel steel connector and compared the results with those of a monolithic joint. Their results showed that all the specimens presented similar failure modes, and that the length of the steel plate in the beam could affect the maximum bearing capacity of the joint. Zhang et al. (2020b) tested seven precast RC beam-column joints with different end-plate connections to show that their proposed connection not only exhibited better mechanical behaviours but also made construction more convenient. In addition, Ghayeb et al. (2020) designed three novel hybrid precast reinforced concrete beam-column connections for high-rise buildings and tested five half-scale joints under cyclic loading. The connections used steel tubes, steel plates and steel couplers to join beams and columns. Their results showed that hybrid connections could improve flexural crack resistance and meet the requirements of seismic codes. Thus, the effectiveness of steel plate connections between beams and columns has been proven to be acceptable (Shufeng et al. 2018; Zhang

et al. 2020a). However, the existing studies focus on only the application of the steel plate connections used in the precast beam-column joints. There are few studies about the application of the steel plate connections used in other kinds of joints, for example, diaphragm wall–waler beam–strut joints. Generally, the wall–beam–strut joints are connected by embedded steel couplers to ensure the continuity of the reinforcements. However, due to construction errors related to the depth of the diaphragm wall trench and vibrations of the concrete, the embedded steel couplers often deviate from the original design position or even are losted sometimes, which is inconvenient during constructions. To overcome these problems, a welded steel plate connection was proposed in this paper. To investigate whether the proposed welded steel plate connection can meet the design requirements of the prefabricated underground construction, this article presents an experimental study on the mechanical behaviour of a wall–beam–strut joint using a steel plate connection under monotonic loading and cyclic loading. Four full-scale specimens are tested, two of which use a steel coupler connection, while the other two joints are connected by steel plates. The mechanical behaviour of the joints in terms of the failure mode, crack distribution, bearing capacity, stiffness, reinforcement strains, and hysteretic behaviour are discussed.

2 Welded Steel Plate Connection Method for Prefabricated Underground Constructions

Figure 1 shows a new prefabricated underground metro station, which is currently under construction in Guangzhou. New metro station prefabrication can be used in combination with the cut-and-cover method, in which the diaphragm wall, waler beam, pillar, top beam with openings and some connections are cast-in-place while the platform slab, strut and concrete slab between struts are precast. To avoid waste and demolition, this temporary supporting system is designed to be a part of the permanent station structure, which is partly prefabricated. Therefore, as parts of the internal support system, the precast struts and pillars are also parts of the permanent components of the metro station after being combined with the cast-in-place concrete. In addition, as the diaphragm wall is a part of the station permanent framework, it must retain the soil and water around the metro station. Generally, the wall–beam–strut joints, as shown in Fig. 2, are connected by embedded steel coupler connections to ensure the continuity of the reinforcements. However, the challenges of the current wall-to-beam joint are that the embedded mechanical couplers easily deviate from the original design position because of the construction error related to the depth of the diaphragm wall trench and the vibration of the concrete. Once the deviation of the mechanical couplers from the original design position exceeds the construction tolerance, post-installed reinforcing methods are needed, which is inconvenient for construction. To overcome the aforementioned problems, a welded steel plate connection method was proposed in this study. As shown in Fig. 3, upper and lower vertical steel plates are embedded into the diaphragm wall, and after the construction of the wall, horizontal steel plates are jointed with the vertical steel plates by welding. Because of the width of the vertical steel plates, the proposed connections can provide additional construction tolerances. To investigate the safety of the proposed joints and the differences in mechanical performance compared with that of the steel coupler connections, four full-scale tests were conducted in this paper. The findings may provide scientific bases and valuable suggestions for the design of the proposed joints for the prefabricated underground constructions.

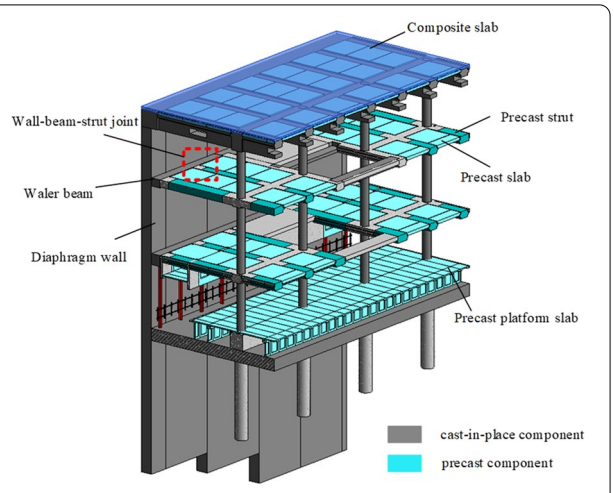

Fig. 1 Configuration of a new prefabricated metro station.

3 Experimental Testing Programme

3.1 Details of the Specimens

To investigate the mechanical behaviour of the welded steel plate connection joint, four full-scale joint specimens were designed and constructed according to the Chinese "Code for design of concrete structures (GB50010-2010)" and "Code for seismic design of buildings (GB50011-2010)". All the specimens have the same geometry and size and consist of three parts, namely, the diaphragm wall, waler beam and strut, which are shown in Figs. 4 and 5. Specimens P1 and P2 adopt welded steel plate connections and are tested under monotonic and low-reversed cyclic loading conditions, respectively, while specimens C1 and C2 adopt mechanical coupler

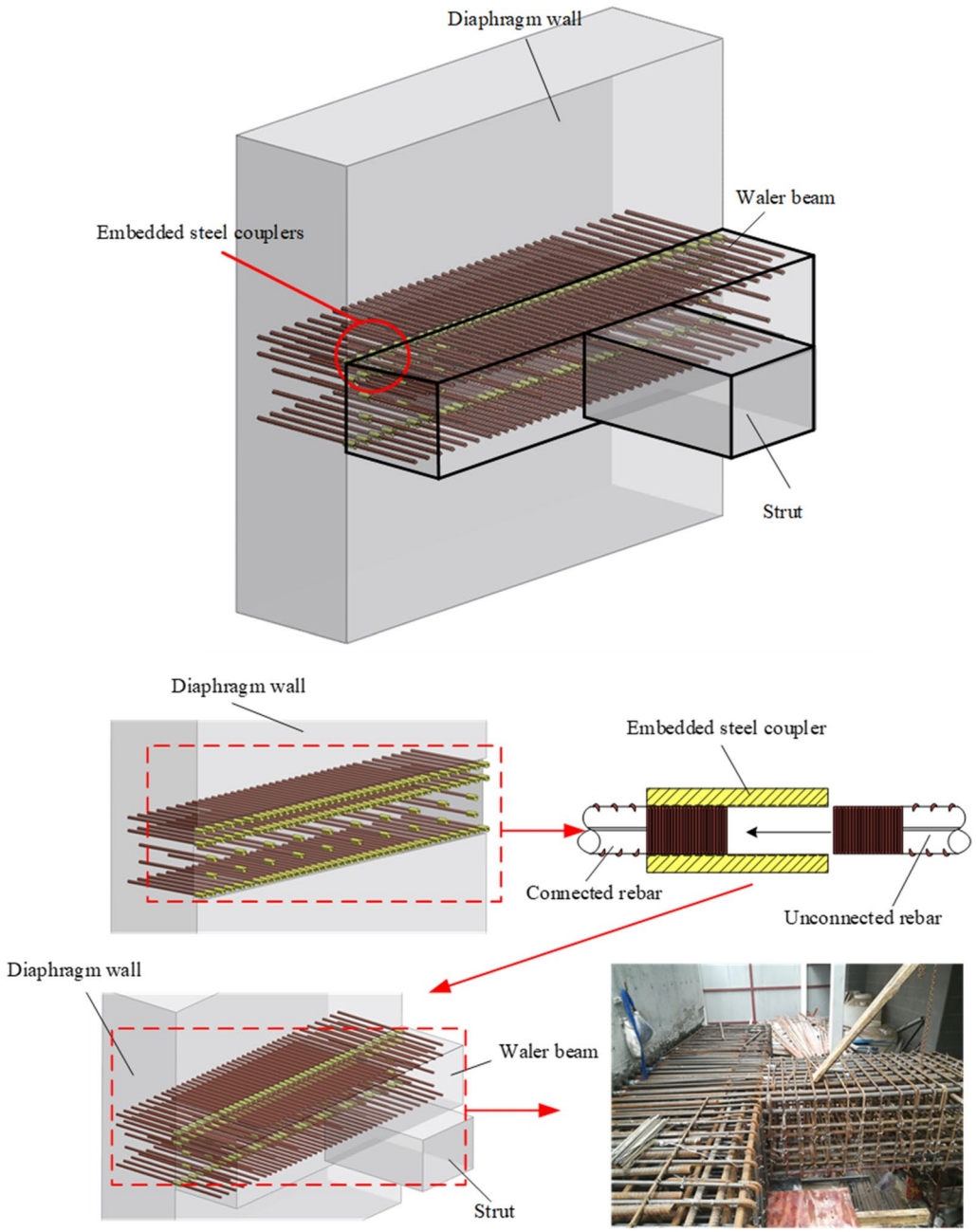

Fig. 2 Embedded steel coupler connections.

connections and are tested in the same way to compare their mechanical behaviours with those of the specimens with welded steel plate connections.

The welded steel plate connection of specimens P1 and P2 is depicted in Fig. 6, in which the upper and lower vertical steel plates with a thickness of 30 mm are embedded into the diaphragm wall and welded with two rows of anchor bars. Moreover, additional upper and lower horizontal steel plates with the same thicknesses are also used and welded to the upper and lower vertical steel plates, respectively. Furthermore, the L-shaped reinforcement bars in the waler beam are connected to the horizontal steel plates by groove welding, and the ends of the L-shaped rebar are double-welded butt joints, which guarantees an effective connection between the wall and beam. The reinforcement bars between the

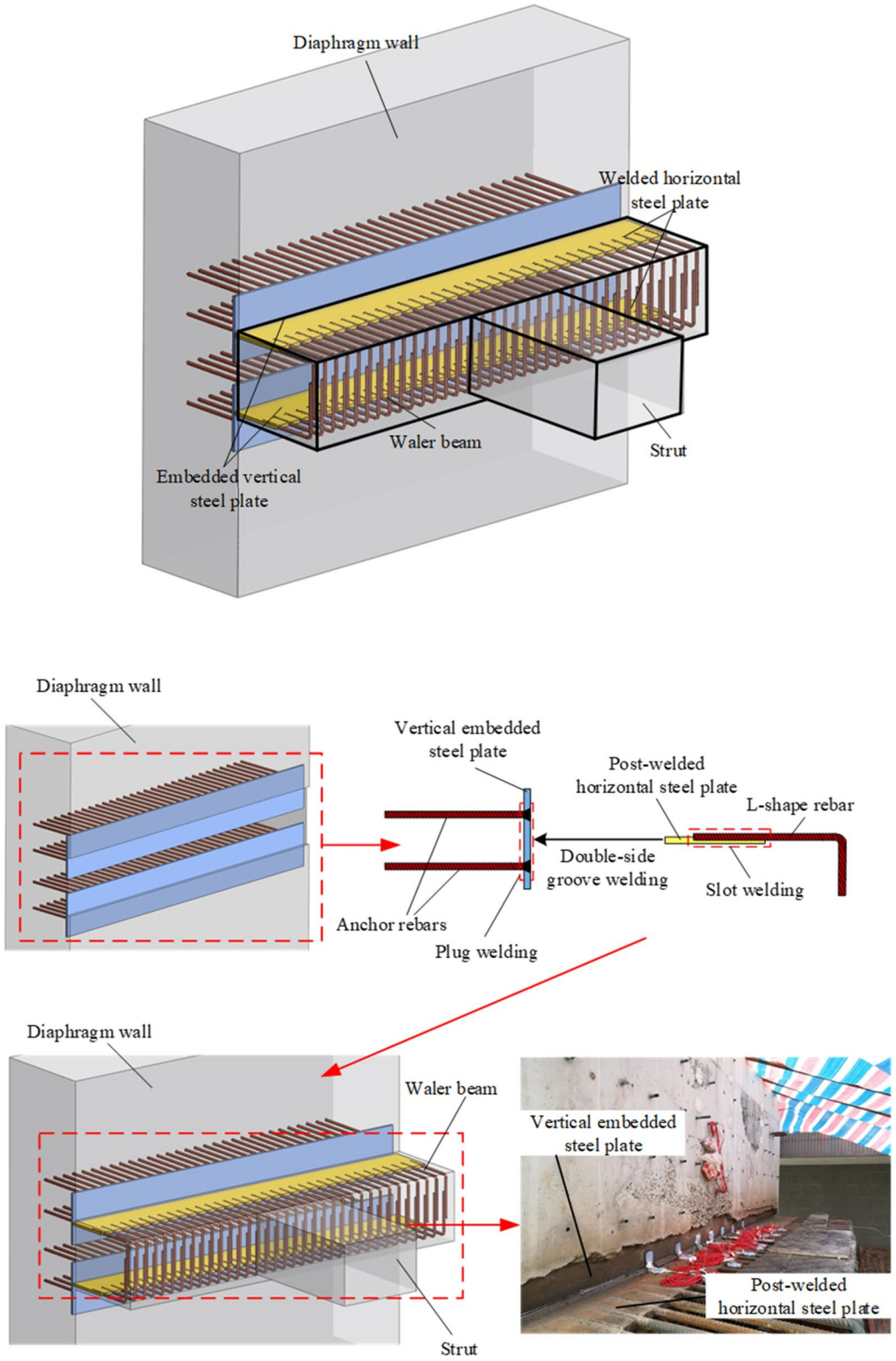

Fig. 3 Welded steel plate connection.

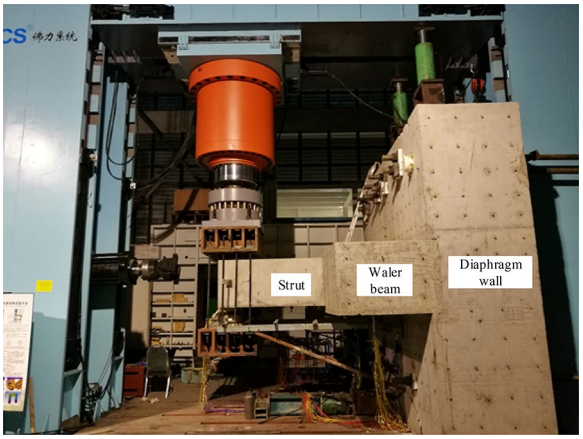

Fig. 4 Configuration of a wall–beam–strut joint.

beam and the strut are lap splices. The mechanical couplers used in specimens C1 and C2 are shown in Fig. 7, in which five rows of mechanical couplers are embedded in the diaphragm wall and are used to connect the rebar in the waler beam. In terms of the configuration of the reinforcements in the strut, two rows of tensile reinforcements with a diameter of 32 mm are placed in the top area of the cross-section while one row of compressive reinforcements with the same diameter are installed in the bottom. The diaphragm wall was poured using underwater concrete, but the waler beam and the strut were poured with commercial concrete. In addition, the waler beam and the strut were poured later than the wall, which generated a cold joint between the wall and the beam. All the longitudinal rebar and hoops of the specimens were HRB400, which means that the characteristic yield strength of the rebar was 400 MPa according to the Chinese code "Steel for the reinforcement of concrete (GB/T 1499.2-2018)". Furthermore, the tensile strength of the mechanical coupler was no less than 1.1 times the tensile strength of the connecting rebar according to the Chinese code "Technical specification for mechanical splicing of steel reinforcing bars (JGJ 107-2016)". The measured mechanical parameters of the concrete and rebar are listed in Table 1.

3.2 Test Setup and Instrumentation

In this experimental investigation, all the tests were carried out in the State Key Laboratory of Subtropical Building Science at South China University of Technology. As shown in Figs. 4 and 8, an electrohydraulic servo multifunction structure testing system was used to conduct the experiments. An electrohydraulic servo actuator, with a + 20,000 kN (− 5000 kN) force capacity and ± 600 mm displacement range, was placed at the end of the strut, which could exert monotonic loading and low-reversed cyclic loading. In addition, two hydraulic jacks were set on the top of the diaphragm wall, which was connected to the reaction frame with steel rods, avoiding sliding and overturning of the specimens. A series of measuring

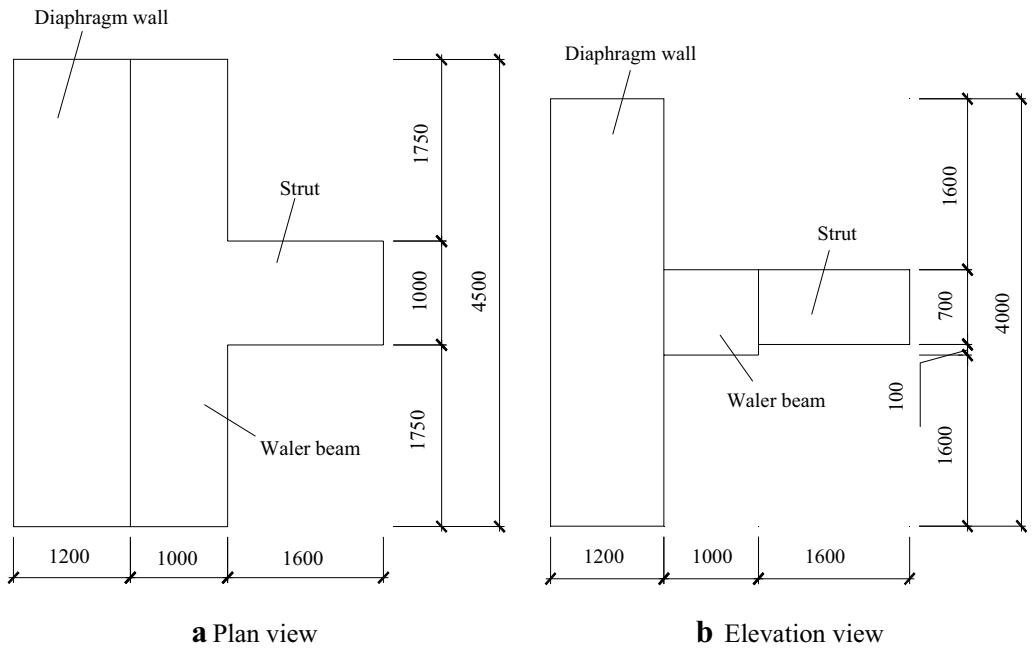

Fig. 5 Geometry and size of the specimens (unit: mm).

a Configuration of a wall-beam joint connected by welded steel plates

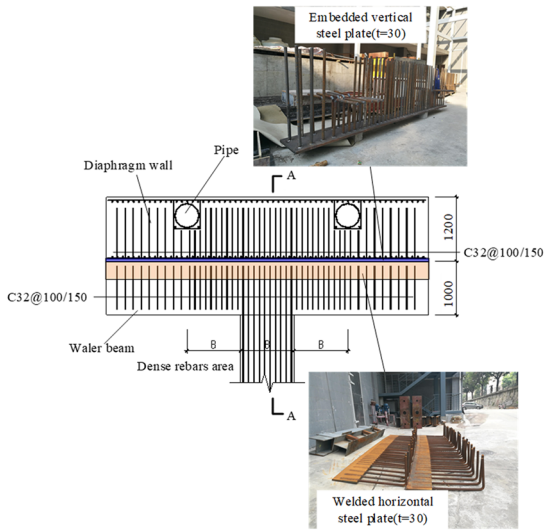

b Vertical view of the wall-beam joint connected by the welded steel plate

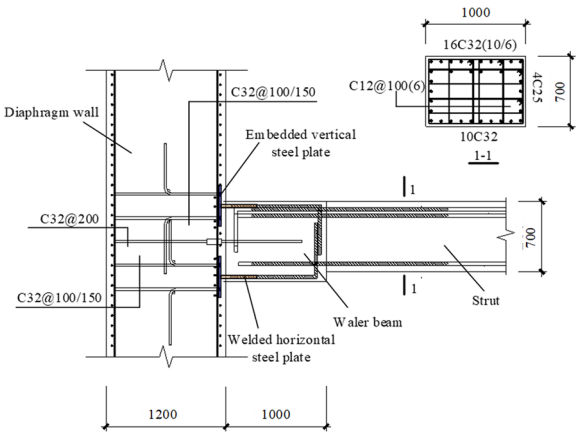

c Cross section of A-A

Fig. 6 Details of specimens P1 and P2 (unit: mm).

a Configuration of a wall-beam joint connected by mechanical couplers

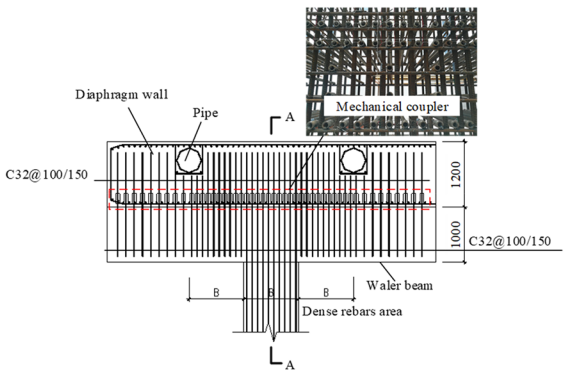

b Vertical view of the wall-beam joint connected by mechanical couplers

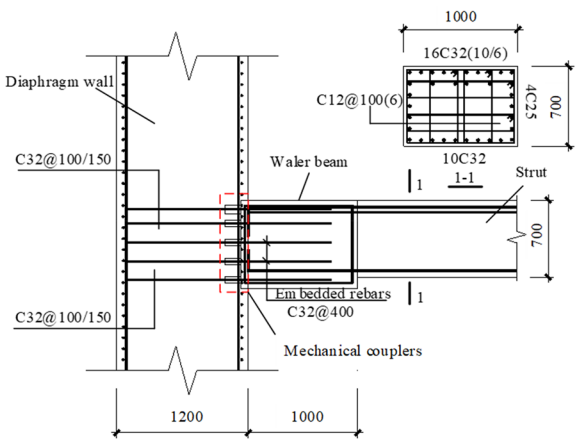

c Cross section of A-A

Fig. 7 Details of specimens C1 and C2 (unit: mm).

apparatuses was utilized to measure and record the strain, deformation and load, as shown in Fig. 9. Some linear variable displacement transducers (LVDTs) were installed under the strut and the waler beam to measure the deformation. LVDTs #1 to #4 were used to measure the deformation of the strut, in which LVDT #1 was installed to calculate the vertical displacement of the loading point. LVDTs #5 and #6 were installed to record

Table 1 Measured mechanical parameters.

Specimen	Concrete		Reinforcement bar		Steel plate	Mechanical couplers
	Wall	Beam and strut				
	f_c (MPa)	f_c (MPa)	f_y (MPa)	f_u (MPa)	f_{ys} (MPa)	f_{yc} (MPa)
P1	41.1	37.4	436.3	577.8	345	–
C1	52.4	40.0	445.8	571.5	–	495
P2	44.3	37.7	437.3	565.3	345	–
C2	50.3	38.4	446.5	571.0	–	495

f_c; f_y; f_u; f_{ys}; and f_{yc} are the cubic compressive strength of the concrete, yield strength of the rebar, ultimate strength of the rebar, yield strength of the steel plate, and yield strength of the mechanical coupler, respectively. The data in the above table are the average values of all measured data.

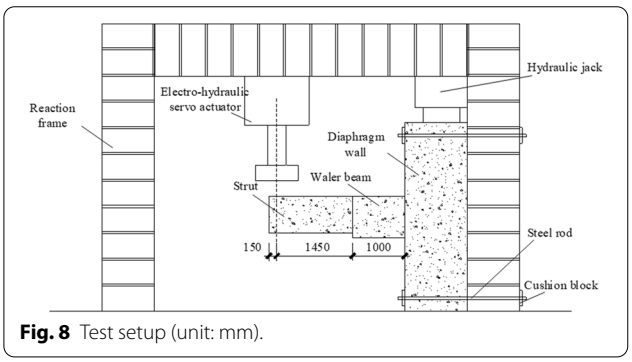

Fig. 8 Test setup (unit: mm).

the vertical displacement of the waler beam. Moreover, some strain gauges were attached to the longitudinal rebar and steel plate to measure the uniaxial strains and reveal the plasticity development process.

3.3 Loading Regimen

3.3.1 Monotonic Loading Regimen

Before the specimen yields, the load increment is increased from zero in 10% increments of the cracking load (F_{cr}). After the specimen yields, the load incrementally increases until specimen failure occurs. According to the standard for the test methods of concrete structures (GB/T 50152-2012), when the concrete in the compressive zone crushes the specimen loses its bearing capacity.

3.3.2 Low-Reversed Cyclic Loading Regimen

The cyclic loading pattern adopted in the test is shown in Fig. 10. The Chinese specification for the seismic testing of buildings (JGJ/T 101-2015) is taken as a guideline for the loading pattern. Low-reversed cyclic loading tests, i.e., so-called pseudostatic tests, are conducted to evaluate the seismic behaviour of the specimen. In this work, a specimen is subjected to the repeating loading and unloading conditions shown in Fig. 10, which could simulate the loading conditions of the specimen during an earthquake. Load control is applied from the beginning of loading until the yield load and was followed by displacement control until failure. Based on the relevant requirements in the guideline, in the load control stage, the load amplitude of the first loading cycle equals 0.6 times the yield load, while that of the second loading cycle equals 0.8 times the yield load. In the third loading cycle, the amplitude then equals the yield load. After the third loading cycle, the displacement-controlled loading mode starts. The vertical displacement of the strut at the loading point at the time that the specimen yields is defined as the yield displacement (Δy) in the skeleton curve. During the displacement-controlled loading stage, the displacement amplitude increases after every three cycles, and the amplitude increases by 1, 2, and 3 times the yield displacement until the bearing capacity of the specimen decreases to 85% of its ultimate bearing capacity. The speed of the applied load in monotonic and cyclic load tests is controlled to remain slow and stable according to the requirements in the standard for the test methods of concrete structures (GB/T 50152-2012).

4 Testing Results and Analyses

4.1 Mechanical Behaviour of the Wall–Beam–Strut Joints Under Monotonic Loading

4.1.1 Crack Distribution and Failure Mode

The ultimate failure pattern and crack distribution of specimens P1 and C1 with the connections of the steel plates and mechanical couplers under monotonic loading conditions are illustrated in Figs. 11 and 12, respectively. At the beginning of the loading process, for both P1 and C1, the first tensile crack occurred on the top surface of the cross-section between the strut and waler beam. The bending moment caused by the loading was the largest in this cross-section along the strut. As the load increased, some flexural cracks appeared on the side surface of the strut and extended from the top to the bottom of the strut and gradually forming flexural-shear cracks. Meanwhile, an increasing number of tensile

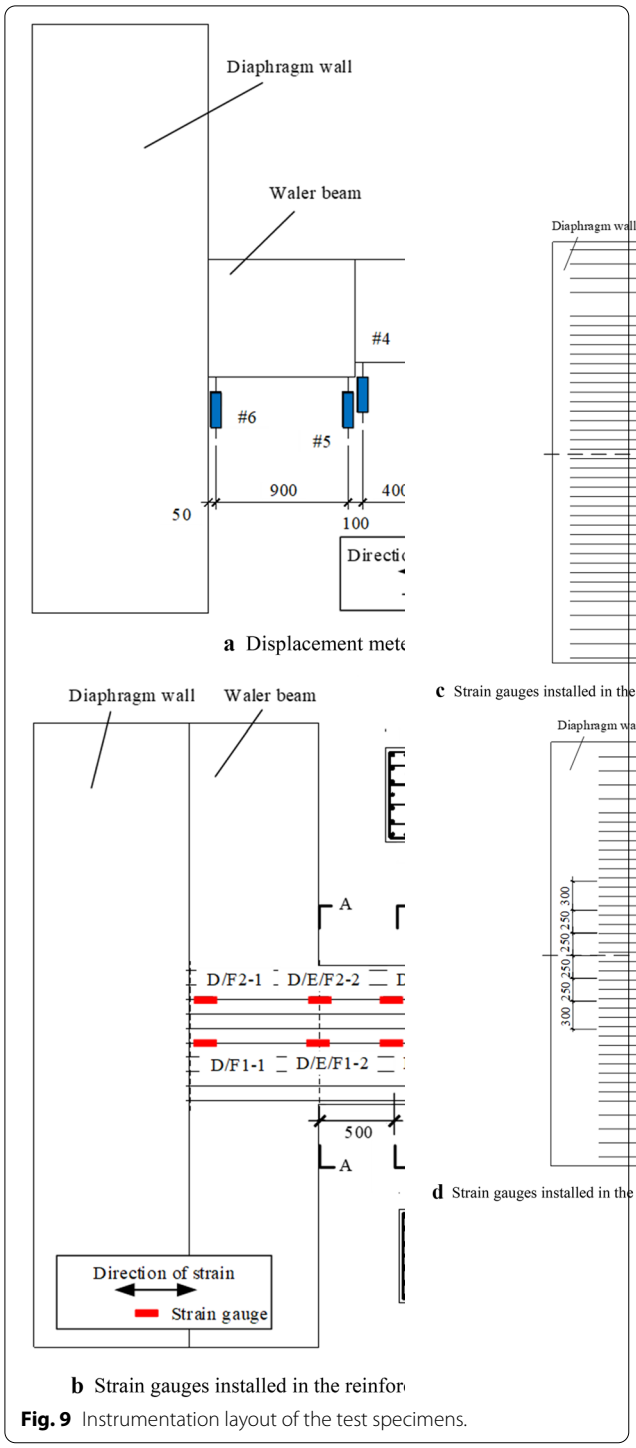

a Displacement mete

b Strain gauges installed in the reinfor

c Strain gauges installed in the reinforcements of the waler beam (specimens C1 and C2)

d Strain gauges installed in the upper steel plate of the waler beam (specimens P1 and P2)

Fig. 9 Instrumentation layout of the test specimens.

horizontal cracks appeared and coalesced on the top surface of the strut, and some semicircular cracks occurred on the top surface of the beam near the edge of the strut. In specimen P1, tensile horizontal cracks appeared on the top surface of the beam, where the edge of the welded steel plate was located. After the specimen yielded, the cracks gradually coalesced, which did not happen in C1. Moreover, the distribution of the semicircular cracks in specimen P1 was denser than that in specimen C1. These phenomena revealed that the welded steel plate could evenly and effectively transfer the load from the strut to the beam. In the final loading stage, the flexural-shear

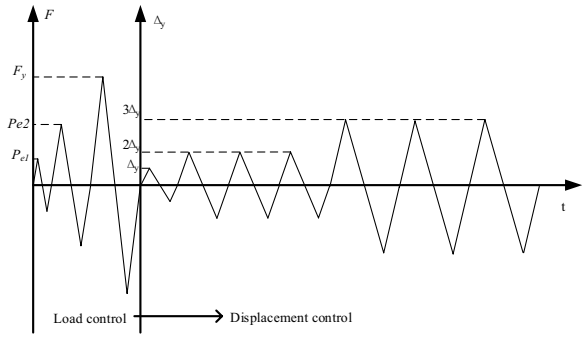

Fig. 10 Low-reversed cyclic loading pattern.

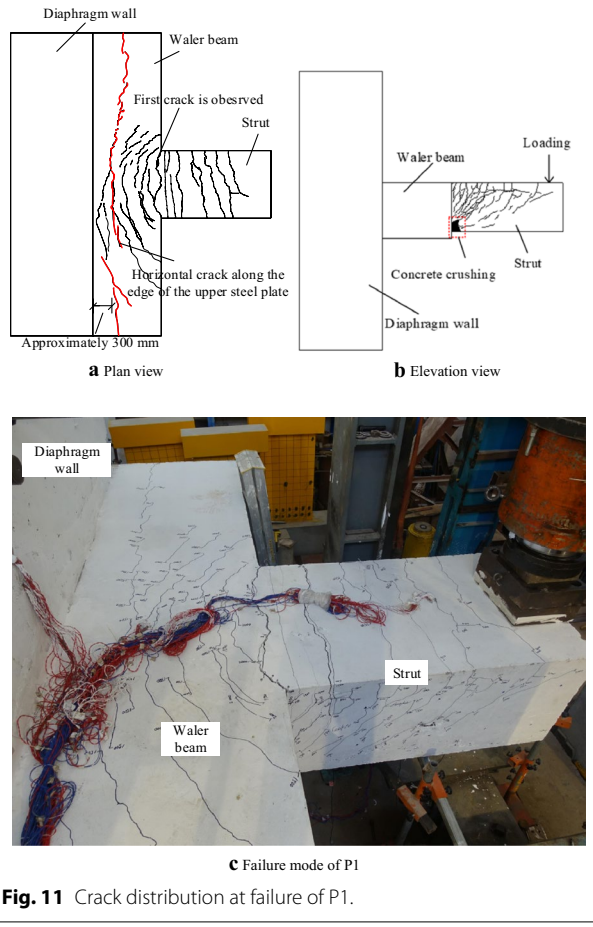

Fig. 11 Crack distribution at failure of P1.

cracks propagated obliquely towards the bottom of the interface between the strut and the beam, and bottom concrete spalling and crushing were observed in this area in both specimens, which indicated that the specimens failed. Hence, the failure modes of the joints were similar and could be considered the shear compression failure in the strut. The similarities and differences in the observed

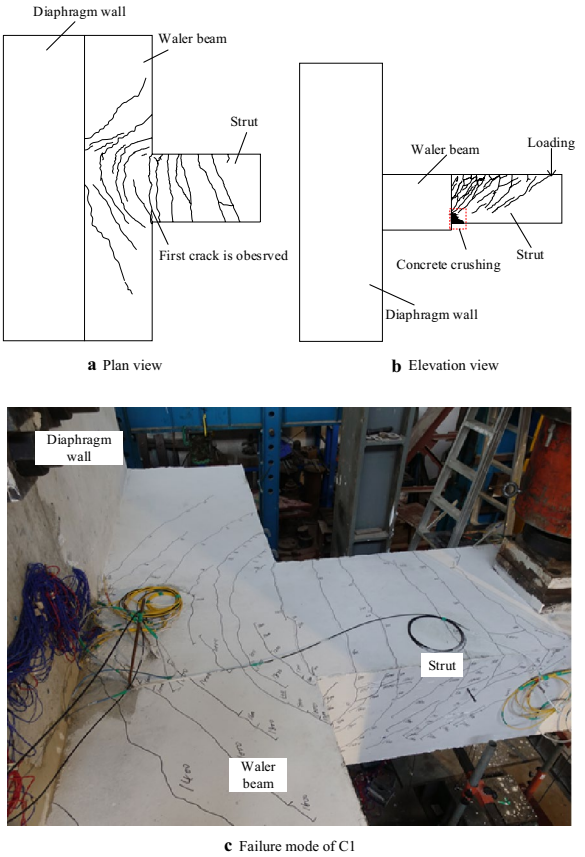

Fig. 12 Crack distribution at failure of C1.

failure characteristics of the samples with the steel plate connection and the steel coupler connection are summarized in Table 2.

4.1.2 Ultimate Bearing Capacity

Figure 13 compares the displacement-loading curves of the two specimens P1 and C1 with the steel plate and mechanical coupler connections, respectively, under monotonic loading conditions. The data monitored from LVDT #1 installed under the bottom of the end of the strut, as shown in Fig. 13, are used to plot the curves. For specimen P1 with the steel plate connection, the first crack appeared when the load reached 280 kN. When the displacement reached 23.8 mm, a yield load of 2350 kN was recorded. As the displacement increased to 79.5 mm, an ultimate load of 2845 kN was reached. For specimen C1 with the mechanical coupler connection, the first cracking load was 240 kN, which was similar to that of P1. Moreover, C1 had a similar yield load of 2200 kN, which was 7% smaller than that of P1. However, when C1 yielded, the displacement reached 28.0 mm, which was 18% larger than that of P1 and revealed that the welded steel

Table 2 Similarities of and differences in the observed failure characteristics of samples P1 and C1 with the steel plate connection and the steel couple connection, respectively.

Specimen	P1 with the steel plate connection	C1 with the steel coupler connection
Similarities	(1) Cracks first form in the interface between the waler and strut (2) As the load increases, the flexural cracks gradually appear to exhibit a shear failure mode and then propagate obliquely towards the bottom of the strut-beam interface (3) The spalling and crushing of the concrete at the bottom of the samples cause the joints to lose their bearing capacities; the shear compression failure of the strut is the failure mechanism	
Differences	(1) Horizontal cracks emerge on the top surface of the waler beam along the edge of steel plate (2) The distribution of semicircular cracks on the surface of the waler beam is denser	(1) No horizontal cracks appear on the top surface of the waler beam

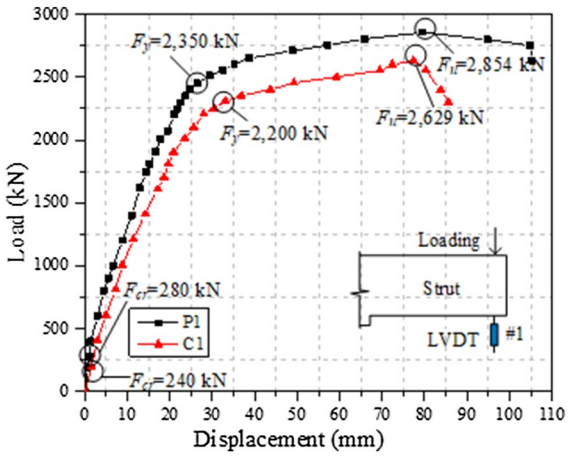

Fig. 13 Displacement–load curve for the monotonic test.

plate in the waler beam could increase the stiffness of the wall–beam–strut joint. In addition, the ultimate load of C1 was 2629 kN, which was 8% smaller than that of P1. Before the specimens yielded, the displacements of both specimens increased linearly as the loading displacement increased. The gradient of the curves reflected the initial stiffness of the specimens. Figure 13 clearly shows that the initial stiffness of C1 was slightly smaller than that of P1, which was also reflected by the different yield displacements. After the specimens reached the yield load, the displacement increased more quickly, although the loading increment was the same. After reaching the ultimate loads, the bearing capacity of both specimens decreased quickly with the load. However, the bearing capacity of P1 decreased more slowly than that of C1. It can thus be inferred that compared to the mechanical coupler connection, the welded steel plate connection can improve the ductile behaviour of the joint, because it can transmit the load to the waler beam more effectively, which was also revealed by the crack patterns discussed above and illustrated in Figs. 11 and 12.

4.1.3 Strain of Reinforcement

The strain of the reinforcement in the strut and waler beam was measured with increasing load and is shown in Figs. 14, 15 and 16. The strain can reflect the actual stress state of the rebar before they yield and indicate, where the plastic area develops in the specimens. As shown in Fig. 14, when the load of specimen P1 reached 1814 kN, the first row of longitudinal reinforcements in the strut yielded at the beam-strut interface according to the monitored strains of D1-2 and D2-2, and the moment in this area was the largest among all the cross-sections of the strut. For specimen C1, the curves of the strains of D1-2 and D2-2 showed similar tendencies. However, yielding loads of the first row of reinforcements were different because of the different yielding strengths of the reinforcements. Compared with the load vs. displacement curves shown in Fig. 13, after cracking, the tensile force in the top area of the strut was mainly borne by the reinforcements and the yielding of the first row of reinforcements did not result in the yielding of the joints. Shortly after the first row of rebars yielded, the second row of longitudinal rebar yielded, as shown in Fig. 15. The yield loads of the second row of reinforcements were close to those of the joints, which indicated that the yielding of the second row of reinforcements caused the yielding of the joint. Figure 16 shows the strain distribution in the waler beam, which revealed that the largest strain in both specimens appeared in the central area of the waler beam. However, when compared with the strain at the edge of the waler beam, the strain in the central area of different specimens showed different results. For specimen P1, notably, although the strain gauges C1-13 and C1-14 were broken, it could be assumed that the strain distribution was axisymmetric. Hence, the largest strain of C1-12 at the centre

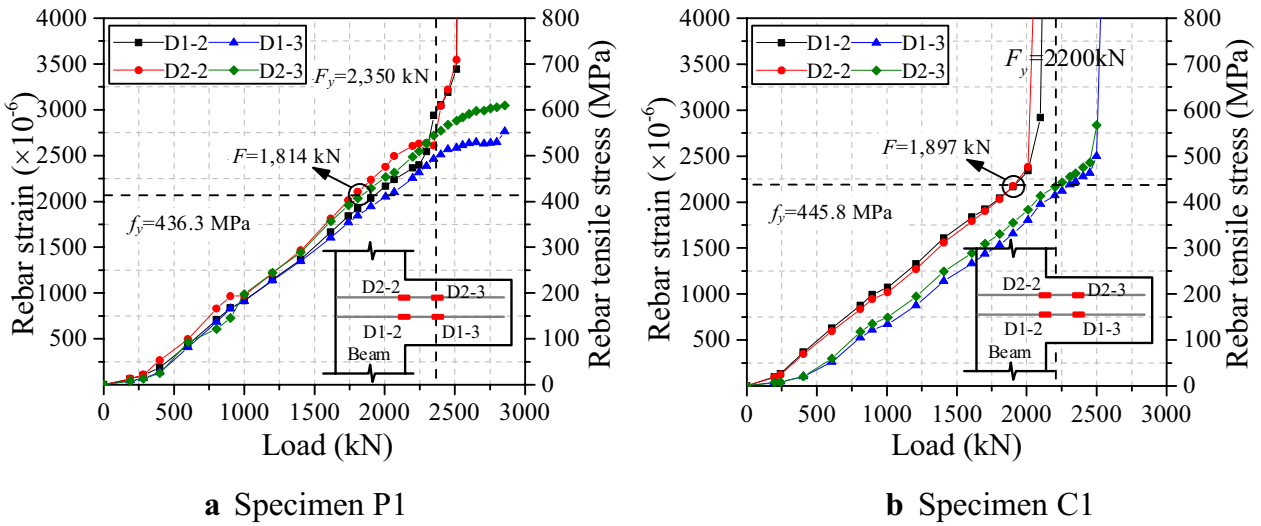

a Specimen P1 **b** Specimen C1

Fig. 14 Strain in the first row of longitudinal rebar in the strut.

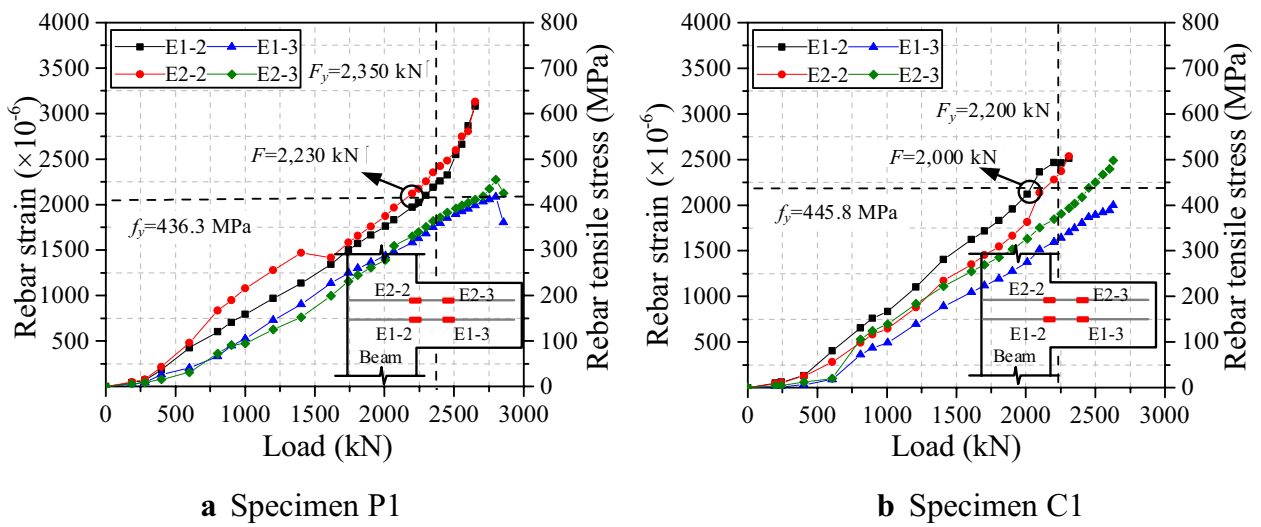

a Specimen P1 **b** Specimen C1

Fig. 15 Strain in the second row of longitudinal rebar in the strut.

was approximately 3 times that of C1-8 at the edge of the beam. The largest strain of C1-6 at the centre was approximately 5 times as that of C1-1 at the edge of the beam in specimen C1. In addition, when the specimens yielded, the steel plate in specimen P1 was still in a relatively low-stress condition, but the central embedded reinforcement in specimen C1 yielded. This result revealed that the horizontal welded steel plate could transmit the load to the specimen more evenly and decrease the stress concentration in the core area compared with that of the mechanical couplers, which also prevented the plastic area from further developing in the beam.

4.2 Mechanical Behaviour of the Wall–Beam–Strut Joints Under Low-Reversed Cyclic Loading

4.2.1 Hysteresis and Skeleton Curve

The ultimate fracture patterns of specimens P2 and C2 are shown in Fig. 17 Both specimens were tested under the low-reversed cyclic loading conditions described in

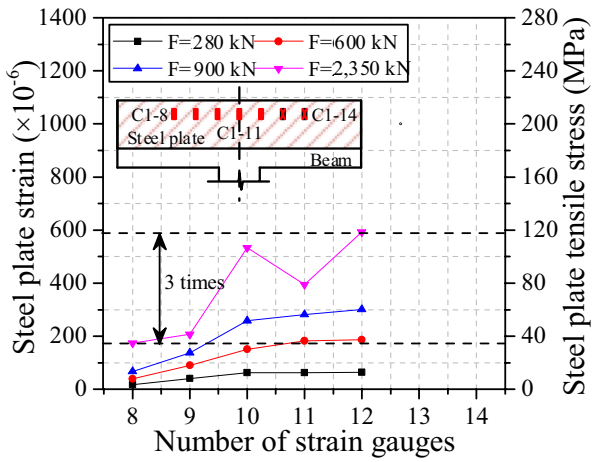

a Upper horizontal welded steel plate of P1

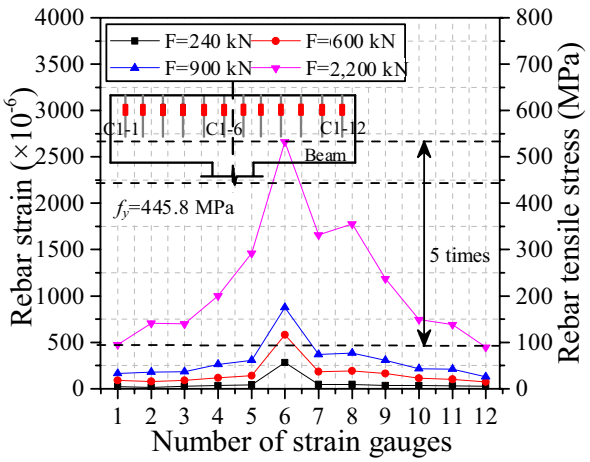

b Frist row of rebar in the beam of C1

Fig. 16 Strain of the welded steel plate/rebar in the beam.

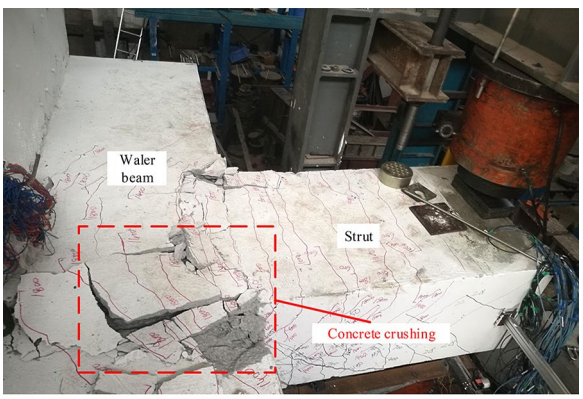

a Specimen C2

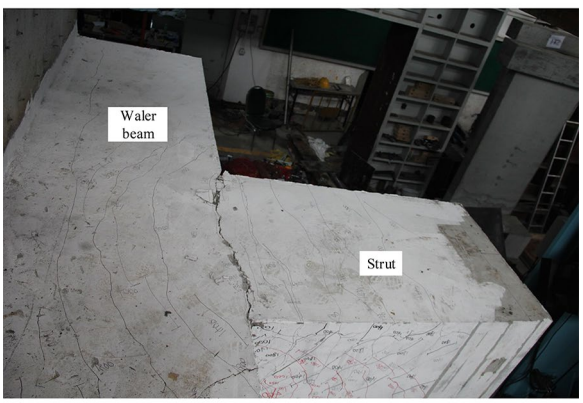

b Specimen P2

Fig. 17 Ultimate fracture patterns of specimens C2 and P2.

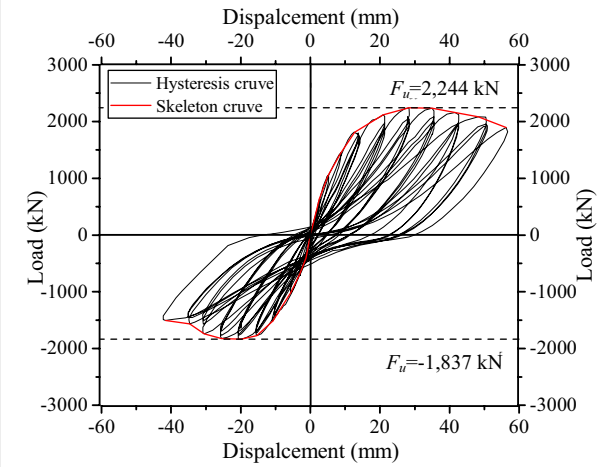

Fig. 18 Hysteresis and skeleton curve of P2.

Sect. 3.3.2, and the displacement at the end of the strut was measured by a displacement sensor. The corresponding hysteresis and skeleton curves of specimens P2 and C2 are shown in Figs. 18 and 19, respectively. Generally, at the beginning of the loading stage, the displacement increased linearly as the load increased. After the specimen yielded, the slippage of the reinforcement in the strut and the development of cracks caused the pinching phenomenon shown in the hysteresis curve. For specimen P2, a peak load of 2244 kN was recorded when the displacement in the positive direction reached 28.3 mm, and the displacement in the negative direction was − 19.8 mm when the peak load reached −1837 kN, as shown in Fig. 18. After the peak load was reached, the

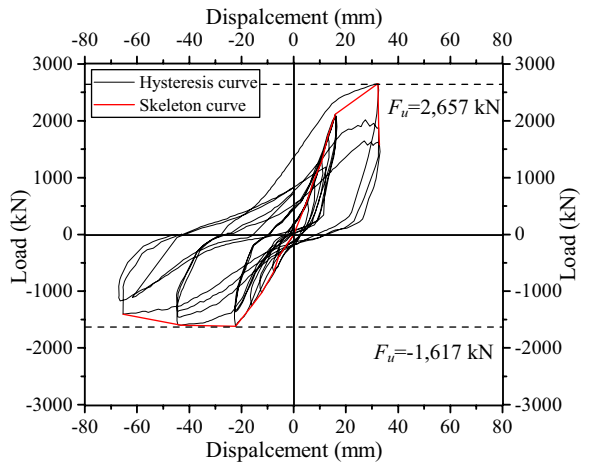

Fig. 19 Hysteresis and skeleton curve of C2.

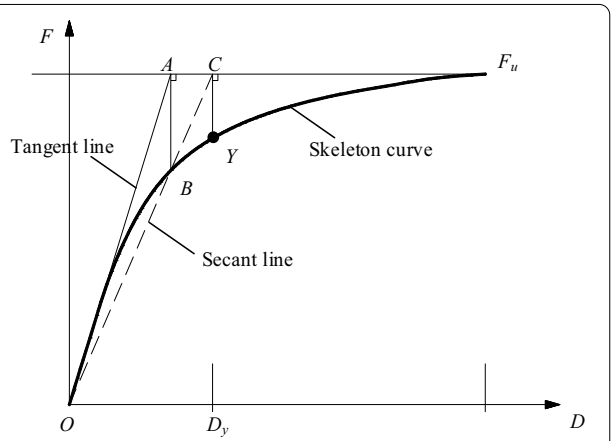

Fig. 20 Geometrograph method for estimating the yield displacement (D_y).

strength of specimen P2 declined slowly in both directions, which meant that the joint had good ductile behaviour. As depicted in Fig. 19, the ultimate load of specimen C2 was 2657 kN in the positive direction, which was 18% larger than that of P2. However, the strength of specimen C2 declined rapidly after it reached the peak load in the positive direction because of the fracture of the reinforcement bar in the top of the strut, which led to the failuring of the specimen. Moreover, in the negative direction, both specimens demonstrated good hysteresis behaviour and similar ultimate bearing capacities.

To further compare the ductile behaviours, the proposed geometric method is used to estimate the yield displacements of the specimens (refer to Fig. 20), and the data are summarized in Table 3. For the positive direction, the displacement ductility coefficient of P2 is 4.04, which is approximately 2 times that of C2. The coefficient in the negative direction of P2 is also larger than that of C2. Thus, it can be inferred that specimen P2 exhibits a stronger hysteresis behaviour in both directions, since the welded steel plate installed in specimen P2 can prevent the rebar from slipping in the waler beam, which restrains the development of the plasticity area.

According to the definitions of the geometrograph method, the yield displacement is the loading displacement at the yield point on the skeleton curve (refer to Fig. 20); the ultimate displacement is the loading displacement at the load point when the declining load equals 85% of the ultimate load; and the displacement ductility coefficient is the ratio of the ultimate displacement to the yield displacement.

4.2.2 Degradation of the Specimen Stiffness

Under cyclic loading, the displacement of the specimen increases as the loading cycle increases, although the peak load remains constant. This represents the deterioration of the specimen stiffness, which was caused by accumulative damage under cyclic loading. The stiffness of the specimen can be equally described by the secant stiffness. The secant stiffness (K_i) is expressed by Eq. (1), and the calculation results are shown in Fig. 18:

$$K_i = \frac{|F_i| + |-F_i|}{|\Delta_i| + |-\Delta_i|} \tag{1}$$

where K_i is the secant stiffness in the ith loading cycle, F_i and $-F_i$ are the peak loads of the ith loading cycle in the positive and negative directions, respectively; Δ_i and $-\Delta_i$ are the peak displacements of the ith loading cycle in the

Table 3 Statistics of the low-reversed cyclic loading results.

Specimen	Load direction	Yield displacement (mm)	Yield load (kN)	Ultimate displacement (mm)	Peak load (kN)	Displacement ductility coefficient
P2	Positive (+)	13.8	1853	55.8	2244	4.04
	Negative (−)	− 10.4	− 1480	− 35.6	− 1837	3.42
C2	Positive (+)	15.9	2117	32.4	2657	2.04
	Negative (−)	− 22.2	− 1616	− 65.4	− 1617	2.95

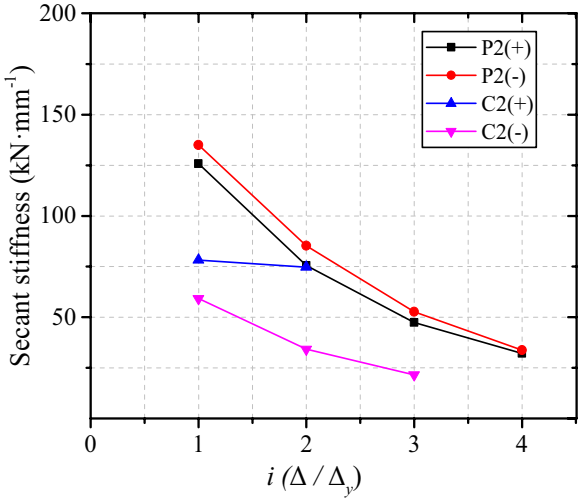

Fig. 21 Degradation of the specimen stiffness.

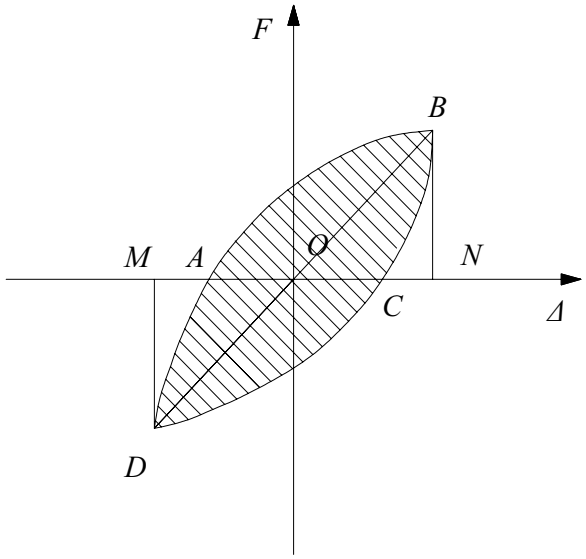

Fig. 22 Definition of the equivalent viscous damping ratio.

positive and negative directions, respectively; and i is the number of cycles.

As Fig. 21 shows, during the early loading process when $i = 1$, the initial secant stiffness of specimen P2 is higher than that of C2 in both directions, which reveals that the welded steel plate can distribute the internal force in the waler beam more evenly than that of the mechanical couplers, with the plate itself acting as an integral part. When $i = 2$, the secant stiffness of P2 seems to deteriorate more severely than that of C2. After i reaches 2, the degradation rate for both specimens becomes flatter and similar. The remaining stiffness of P2 is still higher than that of C2 even if the degradation of the stiffness of P2 is more severe. Moreover, it should be noted that specimen C2 failed suddenly when the third cyclic load in the positive direction was increasing because of the fracture of the reinforcement in the strut. Therefore, the number of cycles for specimen C2 is less than that of specimen P2.

4.2.3 Equivalent Viscous Damping Ratio

The equivalent viscous damping ratio is a very significant parameter for estimating the energy dissipation capacity of a specimen and was proposed by Jacobsen (1930) in 1930. The definition of the equivalent viscous damping ratio is shown in Fig. 22 and can be calculated by Eq. (2):

$$h_e = \frac{1}{2\pi} \cdot \frac{S_{\Delta ABCD}}{S_{\Delta OBN} + S_{\Delta ODM}} \tag{2}$$

where h_e is the equivalent viscous damping ratio; $S_{\Delta ABCD}$ is the area of the enclosed hysteresis loop (ABCD); and $S_{\Delta OBN}$ and $S_{\Delta ODM}$ are the areas of triangles OBN and ODM, respectively.

Figure 23 depicts the calculated equivalent viscous damping ratios of specimens P2 and C2 under low-reversed cyclic loading conditions, which shows that the specimens have similar energy dissipation capacities in both directions when they yield. However, as the load increases, the energy dissipation capacity of specimen C2 increases more rapidly than that of P2, which could indicate that more severe slippage of the reinforcements occurs in C2. The slippage of the reinforcements in the specimen can cause the pinching phenomenon in the hysteresis curve shown in Figs. 18, 19, and significantly affects h_e. Therefore, the rebar-slip in specimen C2 causes an increase in its energy dissipation. Moreover, when

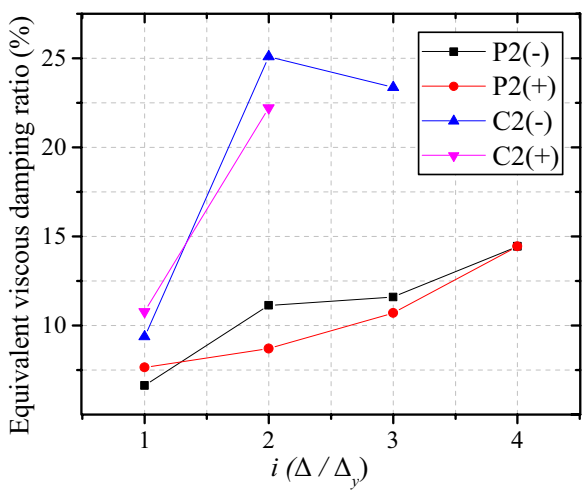

Fig. 23 Equivalent viscous damping ratio of the specimens.

specimen C2 reached 3 times the yield displacement in the negative direction, h_e deteriorated, and the specimen failed after this cycle, which revealed that before specimen failure, the energy dissipation capacity decreased. For specimen P2, the increment in h_e is relatively flat, which indicates that the welded steel plate can both avoid slippage because of its stiffness and improve the specimen's ductile behaviour.

5 Discussion

5.1 Theoretical Flexural Capacity of the Joints

Based on the testing results, the crushing of the concrete in the bottom of the cross-section between the strut and the waler beam caused the failure of the joints. Hence, the cross-section between the strut and the waler beam was selected as the controlling cross-section for further analyses. The yielding and ultimate bending strengths of the joints were discussed in this section using the method recommended by the corresponding code for the design of concrete structures (GB 50010-2010). The following assumptions were made:

1. The cross sections of the reinforced concrete remain as planes before the failure of the reinforced concrete (i.e., plane section assumption).
2. The tensile strength of the concrete may be ignored and the ultimate concrete compressive strain is $\varepsilon_{cu} = 0.0033$. The compressive stress–strain curves follow the model proposed by Rüsch (1960).
3. The constitutive model of the reinforcements follows the bilinear model, which considers the hardening modulus of the reinforcements to be 0.01 times Young's modulus.

As shown in Fig. 24, based on the fibre beam method, the concrete in the cross-section is divided into several fibres of equal height along the height of the section, and the reinforcements with the same height in the section are considered one fibre. The distances between the neutral axis and the centroid of each fibre are then calculated. Based on assumption (1), the strain distribution along the height of the section can be calculated once the rotation angle θ and the neutral axis are confirmed. Furthermore, the stress corresponding to each fibre can be calculated. Therefore, Eq. (3) can be established according to the force equilibrium:

$$N = \sum_{i}^{n} \sigma_{ci} \Delta L b + \sum_{i}^{ns} \sigma_{si} A_{si} = 0 \tag{3}$$

where N is the total axis load of the section, n is the number of concrete fibres, σ_{ci} is the stress corresponding to the ith concrete fibre, ΔL is the height of each concrete fibre, b is the width of the section, ns is the number of

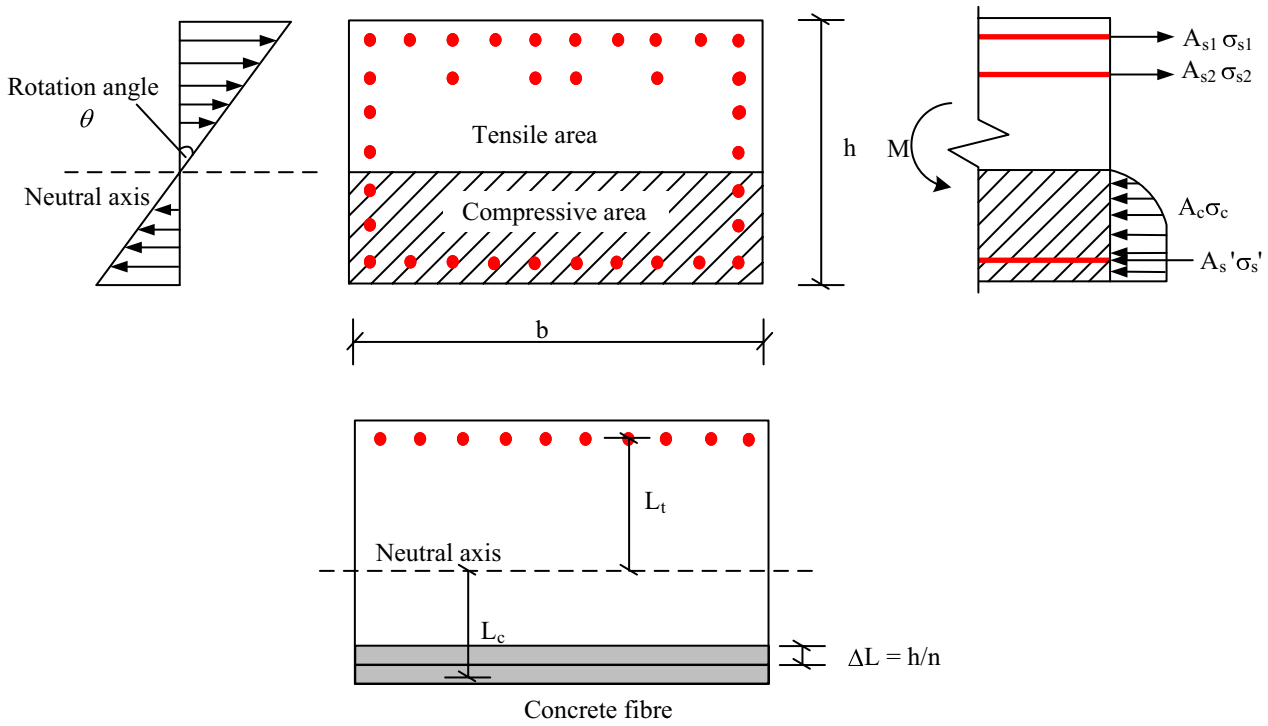

Fig. 24 Calculation diagram of the flexural capacity of the strut's positive section.

reinforcements, σ_{si} is the stress corresponding to the ith reinforcement fibre, and A_{si} is the reinforcement area corresponding to the ith reinforcement fibre.

Equation (4) is obtained from the moment equilibrium:

$$M = \sum_{i}^{n} \sigma_{ci} \Delta L b L_i + \sum_{i}^{ns} \sigma_{si} A_{si} L_i \quad (4)$$

where L_i is the distance between the neutral axis and the centroid of the corresponding fibre. A MATLAB program is developed to solve Eqs. (3), (4). The rotation angle θ is considered the independent variable, and the initial neutral axis is set as the central height of the section. Based on Eq. (3), a binary search program is used to iterate to calculate the true height of the neutral axis. Then, the bending moments of the section can be calculated by Eq. (4). These theoretical results are compared with those from the experimental tests in Table 4.

The results listed in Table 4 show that the theoretically calculated flexural capacities of the specimens under monotonic loads correspond well to the experimental results. Moreover, according to the strain distribution under the ultimate moment, the strain in the compression edge reaching the concrete ultimate compressive strain ε_{cu} results in the failure of the joint, which agrees well with the experimental testing results. The calculation errors for both specimens C1 and P1 are no more than 7%. However, for cyclic tests, the calculation errors and theoretical values are larger than the corresponding experimental results, since the proposed calculation method cannot take into account the accumulative damage of the concrete occurring in the cyclic tests. Notably, when specimen C2 was subjected to the displacements corresponding to two yielding displacements in the positive direction, some reinforcements fractured suddenly. Hence the accumulative damage of the concrete was small and the calculation errors in the positive direction for specimen C2 were thus relatively small.

5.2 Failure Mechanisms and Design Recommendations

The failure modes of the specimens with the two kinds of connections under monotonic loading were similar and could be considered shear compression failure of the strut. Thus, both types of connections can avoid failure from occurring in the wall–beam interface, which prevents the vertical support members from losing their strengths and meets the "strong column, weak beam" design concepts. However, their ultimate bearing capacity and cracking distributions were different. The failure of both specimens began from the yielding of the upper rebar in the strut and ended due to the crushing of the bottom concrete. The ultimate bearing capacity of specimen P1 was 8% higher than that of C1. In addition, the cracking distributions of specimen P1 were more disperse than those of C1, and a horizontal crack, which was parallel to the edge of the upper horizontal steel plate, was observed. Therefore, it can be concluded that the embedded steel plate could transfer the loading to the waler beam more effectively and distribute the loading more evenly than the mechanical couplers could for the prefabricated subway station under static loads. Moreover, the specimens with the two kinds of connections under the low-reversed cyclic loading showed that the joint with the welded steel plate exhibited a better ductile behaviour, since the integrity of the steel plate could avoid the slippage of the rebar in the beam. Correspondingly, the joint connected with mechanical couplers had relatively unsatisfactory ductile behaviour, especially under loading in the positive direction. This was likely caused by the fracturing of the reinforcement bars, consistent with the findings of Aaleti et al. (2012). Overall, the results demonstrated the effectiveness and safety of the connection using the welded plate under both static

Table 4 Comparison between the results from the experimental test and the theoretical calculation.

Type of load	Monotonic load		Cyclic load			
Specimen	P1	C1	P2		C2	
Load direction	Positive (+)	Positive (+)	Positive (+)	Negative (−)	Positive (+)	Negative (−)
Experimental yield moment $M_{ye}=F_y$*1.45 (kN m)	3408	3190	2.687	− 2150	3070	− 2343
Theoretical yield moment M_{yt} (kN m)	3320	3412	3300	− 2667	3430	− 2724
Error $\frac{M_{ye}-M_{yt}}{M_{ye}}$	2.57%	− 6.96%	− 22.82%	− 24.03%	− 11.74%	− 16.25%
Experimental ultimate moment $M_{ue}=F_u$*1.45 (kN m)	4138	3812	3254	− 2664	3853	− 2345
Theoretical ultimate moment M_{ut} (kN m)	3.862	3.957	3.867	− 2.901	3.947	− 2.947
Error $\frac{M_{ue}-M_{ut}}{M_{ue}}$	6.68%	− 3.80%	− 18.85%	− 8.91%	− 2.45%	− 25.69%

and seismic loading conditions, such as earthquakes. Following this study, some suggestions can be given for the design of practical engineering projects with prefabricated underground construction. The experimental testing results demonstrated that both connection methods could ensure the effectiveness of the connection and satisfy the design requirements with safety coefficients larger than 2. Based on the strain distribution of the waler beam and the strut, it can be assumed that the weakest part is the interface between the waler beam and the strut. Additionally, the observation of a horizontal crack along the edge of the upper horizontal steel plate (shown in Fig. 11a) reflects that a slight tensile stress concentration occurred in this section. Consequently, for the welded steel plate connection joint, the strength of the groove welding between the steel plate and the reinforcements should be designed more carefully. Compared with the stress of central area of the waler beam, the stress of the reinforcement bars in the edge area of the beam is lower, which indicates that the quantity of rebar used in the edge can be reduced properly to save resources.

5.3 Limitations

In this research, a welded steel plate connection was proposed to overcome the disadvantages of the conventional steel coupler connection and make construction easier. However, due to the difference in construction conditions between the laboratory and construction site, the on-site setup speed and cost effectiveness need to be further studied. Since the station in Guangzhou that is designed with the welded steel plate is still under construction, the comparative analysis based on the construction utility and cost at the construction site is a potential topic for future studies. To estimate the mechanical behaviour of the specimen under the most high-risk situation, the axial force was not applied to the diaphragm or the strut, which is not consistent with the stress state of the joint in practice. The existence of axial forces in the strut can restrain the development of cracks, which is beneficial for enhancing the ultimate bearing capacity and ductility of the specimen. The influence of the axial force can be determined through numerical simulations in future work. However, limited by time and funding, this paper represents only the results from testing four specimens with the two connections types of welded steel plates and mechanical couplers under monotonic and low-reversed cyclic loading conditions and their preliminary comparative analyses. In future work, numerical models should be established to verify the experimental results and investigate other factors affecting the mechanical behaviour of the specimen, which could optimize the joint design. Through numerical experiments, the behaviour of the interface between the wall and beam should be further studied, which is beneficial for revealing the internal mechanism causing the differences between different joints. In addition, in future experimental studies, the size of the specimen could be reduced, especially that of the diaphragm wall.

6 Conclusions

In this study, a new welded steel plate connection is proposed to facilitate the construction of diaphragm wall–waler beam–strut joints in prefabricated underground metro stations. Four wall–beam–strut joint specimens including two welded steel plate connection joints and two steel coupler connection joints were fabricated and experimentally tested under monotonic and cyclic loading conditions to investigate their mechanical characteristics under static and seismic loads. The major findings are described as follows:

1. In the monotonic load test, all the specimens fail, because the concrete in the bottom compressive zone crushes under shear and compressive stress. Their failure modes could be considered typical shear compression failure of the strut.
2. The cracking patterns and strain distribution in the waler beam indicate that the welded steel plate can transfer the load from the strut to the beam more effectively than the mechanical couplers can. The steel plate connection can relieve the stress concentration phenomenon in the central area of the waler beam, which prevents the plastic area from extending in the waler beam and then improves the strength and ductility of the joint.
3. In the low-cyclic reverse load tests, the joint connected with the welded steel plate exhibits a better ductile behaviour and a higher stiffness than that connected by the mechanical couplers. The large integral stiffness of the steel plate prevents the plastic area from further developing in the beam. However, the energy dissipation capacity of the welded steel plate connection joint is not satisfactory, because the steel plate reduces the slippage of the rebar.
4. A theoretical method is proposed on the basis of the fibre beam method to predict the bending capacity of the wall–beam-joint. The calculated results using the theoretical method are consistent with those from the experimental tests under monotonic loading, which can provide a reference for further theoretical research.
5. Overall, the proposed steel plate connection joints in this study can not only satisfy the design requirements but also present better mechanical behaviour compared with the conventional steel coupler con-

nection. Moreover, the steel plate connection can overcome the disadvantages of the steel connection and improve the construction tolerance although the on-site setup speed and costing effectiveness need to be further studied.

Acknowledgements
Not applicable.

Authors' contributions
TL, JL and DW planned the experimental programme, performed the experiments, analysed the data, and drafted the paper. JL, HL and DW were in charge of the results analysis and paper writing. All the authors contributed to writing the paper. All authors read and approved the final manuscript.

Authors' informations
Tingjin Liu: Associate Professor, State Key Laboratory of Subtropical Building Science, South China University of Technology, Guangzhou, 510640, China; Associate Professor, South China Institute of Geotechnical Engineering, South China University of Technology, Guangzhou 510640, China; Associate Professor, School of Civil Engineering and Transportation, South China University of Technology, Guangzhou 510640, China.

Jiandong Lu and Di Wang: Master's Student, School of Civil Engineering and Transportation, South China University of Technology, Guangzhou 510640, China.

Hongyuan Liu: Senior Lecturer, School of Engineering, University of Tasmania, TAS 7001, Australia.

Funding
The authors would like to acknowledge the support from the National Natural Science Foundations of China (Grant No. 51678248 and Grant No. 51878296); and the Open Research Fund of the State Key Laboratory of Simulation and Regulation of Water Cycle in River Basin (Grant No. IWHR-SKL-KF201818).

Availability of data and materials
The data in the paper will be supplied upon request.

Competing interests
The authors declare that they have no competing interests.

Author details
[1] State Key Laboratory of Subtropical Building Science, South China University of Technology, Guangzhou 510640, China. [2] South China Institute of Geotechnical Engineering, South China University of Technology, Guangzhou 510640, China. [3] School of Civil Engineering and Transportation, South China University of Technology, Guangzhou 510640, China. [4] School of Engineering, University of Tasmania, Hobart, TAS 7001, Australia.

Received: 19 March 2020 Accepted: 7 October 2020
Published online: 12 January 2021

References

Aaleti, S., Brueggen, B. L., Johnson, B., et al. (2012). Cyclic response of reinforced concrete walls with different anchorage details: Experimental investigation. *Journal of Structural Engineering, 139*(7), 1181–1191.

Choi, H. K., Choi, Y. C., & Choi, C. S. (2013). Development and testing of precast concrete beam-to-column connections. *Engineering Structures, 56,* 1820–1835.

Ding, P., et al. (2018). Force transfer and deformation mechanism of single ring structure of prefabricated subway station. *Journal of Southwest Jiaotong University*. **(In Chinese)**.

Ding, P., et al. (2019a). Optimum design of closed cavity structure for prefabricated metro station. *Journal of Bjing University of Technology, 45*(10), 946–955. **(In Chinese)**.

Ding, P., et al. (2019b). Three-dimensional dynamic response analysis of a single-ring structure in a prefabricated subway station. *Sustainable Cities and Society*. 271–286.

Du, X. L., Liu, H. T., Lu, D. C., Xu, C. S., Luo, F. R., & Li, S. M. (2017). Study on seismic performance of sidewall joints in assembled monolithic subway station. *China Civil Engineering Journal, 50*(4), 38–47. **(In Chinese)**.

Esmaeili, J., & Ahooghalandary, N. (2020). Introducing an easy-install precast concrete beam-to-column connection strengthened by steel box and peripheral plates. *Engineering Structures, 205,* 110006.

Ghayeb, H. H., Razak, H. A., & RamliSulong, N. H. (2020). Seismic performance of innovative hybrid precast reinforced concrete beam-to-column connections. *Engineering Structures, 202,* 109886.

Gibb, A. G. F. (1999). *Off-site fabrication: Prefabrication, pre-assembly and modularization*. Hoboken: Wiley.

Gibb, A. (2007). *Offsite construction industry survey—2006*. London: Build Offsite.

Jacobsen, S. L. (1930). Steady forced vibration as influenced by damping. *ASME Transaction, 52*(1), 169–181.

Jaillon, L., & Poon, C. S. (2009). The evolution of prefabricated residential building systems in Hong Kong: A review of the public and the private sector. *Automation in Construction, 18*(3), 239–248.

Kallolil, J. J., Chakrabarti, S. K., & Mishra, R. C. (1998). Experimental investigation of embedded steel plates in reinforced concrete structures. *Engineering Structures, 20,* 105–112.

Pons, O. (2014). Assessing the sustainability of prefabricated buildings. In *Eco-efficient construction and building materials* (pp. 434–456).

Rüsch, H. (1960). Researches toward a general flexural theory for structural concrete. *Journal of the American Concrete Institute, 57*(1), 1–28.

SCC (The State Council of the People's Republic of China). (2016). *Some opinions of the CPC Central Committee and the State Council on further strengthening the management of urban planning and construction*. Beijing: SCC.

Shufeng, L., et al. (2018). Experimental study of a fabricated confined concrete beam-to-column connection with end-plates. *Construction and Building Materials, 158,* 208–216.

Tao, L., et al. (2019). Shaking table test on seismic response characteristics of prefabricated subway station structure. *Tunnelling and Underground Space Technology*.

Taylor, M. D. (2010). A definition and valuation of the UK offsite construction sector. *Construction Management and Economics, 28*(8), 885–896.

Wang, D. C., Wang, G. F., Qiao, N., & Dai, C. S. (2018). The application and prospect analysis of prefabricated construction in underground engineering. *China Sciencepaper, 13*(1), 115–120. **(In Chinese)**.

Yang, X. R., & Han, Y. Z., (2017). Closed cavity thin-wall components design for prefabricated underground subway structures. In *Geo-Risk Conference 2017: Reliability-Based Design and Code Developments, Denver, USA* (pp. 194–205).

Yang, X. R., & Huang, M. Q. (2018). Research strategies on new prefabricated technology of underground subway station. *China Journal of Urban Rapid Rail Transit, 01*, 78–85. **(In Chinese)**.

Yang, X., Shi, Z., & Lin, F. (2019a). Research on shear capacity and checking method of MT-G-joint for application in prefabricated underground structures. *Advances in Materials Science and Engineering*. https://doi.org/10.1155/2019/4065301.

Yang, X., Shi, Z., & Lin, F. (2019b). Influence of geometrical parameters on performance of grouted mortise and tenon joints for application in prefabricated underground structures. *Advances in Civil Engineering*. https://doi.org/10.1155/2019/3747982.

Zhang, X., et al. (2020a). Experimental study on bolted and anchored beam-to-column joints of prefabricated concrete frames. *Advances in Structural Engineering, 23*(2), 374–387.

Zhang, J., et al. (2020b). Experimental seismic study of precast hybrid SFC/RC beam–column connections with different connection details. *Engineering Structures*, *208*, 110295.

Publisher's Note